Mass Utilization Scaling with Propellant Type on a Magnetically Shielded Hall Thruster

IEPC-2024-766

Presented at the 38th International Electric Propulsion Conference, Toulouse, France
June 23-28, 2024

William J. Hurley* and Benjamin A. Jorns†
University of Michigan, Ann Arbor, MI, 48103, United States

A quasi-0D model of the mass utilization efficiency for a Hall effect thruster is derived and validated with experimental data from a magnetically-shielded Hall thruster operating on multiple propellants. This dataset includes results from previous campaigns on xenon and krypton, and new experimental results gathered on argon and nitrogen. The quasi-0D model is derived by integrating the neutral continuity equation along the length of the thruster channel. Results indicate that with a learned characteristic channel length for the entire data set, the model accurately captures mass utilization trends as a function of a single parameter for all four propellants. The extensibility of the model beyond the range of experimental data is explored, and it is found that the dependence of the mass utilization on discharge voltage and magnetic field strength is consistent with the scaling exhibited by previously-studied Hall thrusters.

I. Introduction

Hall thrusters, the most flown electric propulsion device, are widely used for satellite station keeping, orbit raising, and deep space robotic missions. These quasi-neutral, axisymmetric devices utilize orthogonal electric and magnetic fields to ionize and accelerate a neutral gas to produce thrust. Any non-ionized neutrals represent a loss in possible thrust and thus a decrease in overall device efficiency. To ensure most of the propellant is ionized, Hall thrusters are designed so that the mean free path of ionization for neutral gas is much less than the thruster channel length. Following this criterion, optimally designed Hall thrusters ionize the majority ($\geq$ 90 %) of the input propellant.[1]

Historically, many Hall thrusters have been optimized for xenon propellant. Xenon is widely used because it stores densely, has a large ionization cross section, and has substantial atomic mass — resulting in high thrust to power ratios. While xenon has many desirable properties, it is an extremely rare gas in the Earth's atmosphere which makes it expensive and subject to large price fluctuations. These attributes can make planning a mission with xenon difficult, especially when large quantities are required.

Given these difficulties with xenon procurement, gases like krypton, argon, and nitrogen are increasingly being explored as substitutes. Krypton and argon are more available noble gases and are now widely used in the Starlink constellation.[2] Molecular gases like nitrogen could be harvested in-situ for drag compensation of very low earth orbit satellites.[3] While alternative propellants can have numerous advantages, they typically suffer from poor performance on Hall thrusters designed for xenon.[4,5] This in large part has been attributed historically to their faster thermal velocities and smaller ionization cross sections than xenon, which translate to a reduced probability of ionization in the thruster.

Since the propellant utilization is heavily intertwined with the overall device performance, there is a pressing need to develop improved, first-principles informed universal scaling laws for the physical processes that drive this process for disparate gases. To this end, Su et. al.[6] recently proposed a simplified, 0D scaling law for the dependence of mass utilization with discharge current for both xenon and krypton. The goal of this work is to expand on this model, improving its fidelity and expanding the data set to include operating conditions for a wide range of currents and voltages for both argon and nitrogen.

*PhD Candidate, Aerospace Engineering, Email: wjhurley@umich.edu.
†Associate Professor, Aerospace Engineering, Email: bjorns@umich.edu.

This paper is organized in the following way. In Sec. II, we outline our updated scaling law for the mass utilization efficiency. Then, in Sec. III–IV, we overview the experimental setup and analysis techniques to infer the mass utilization efficiency, and outline the key assumptions for our model. Then, we compare the model predictions to experimental data in Sec. V, followed by a discussion of the key results in Sec. VI.

II. Scaling Law for Mass Utilization

In this section, we motivate a similar scaling law for the mass utilization efficiency to that proposed by Su et. al.[6] To this end, we show in Fig. 1(a) a canonical representation of the Hall thruster principle of operation. In this axisymmetric device, a potential difference is applied between the positive anode and

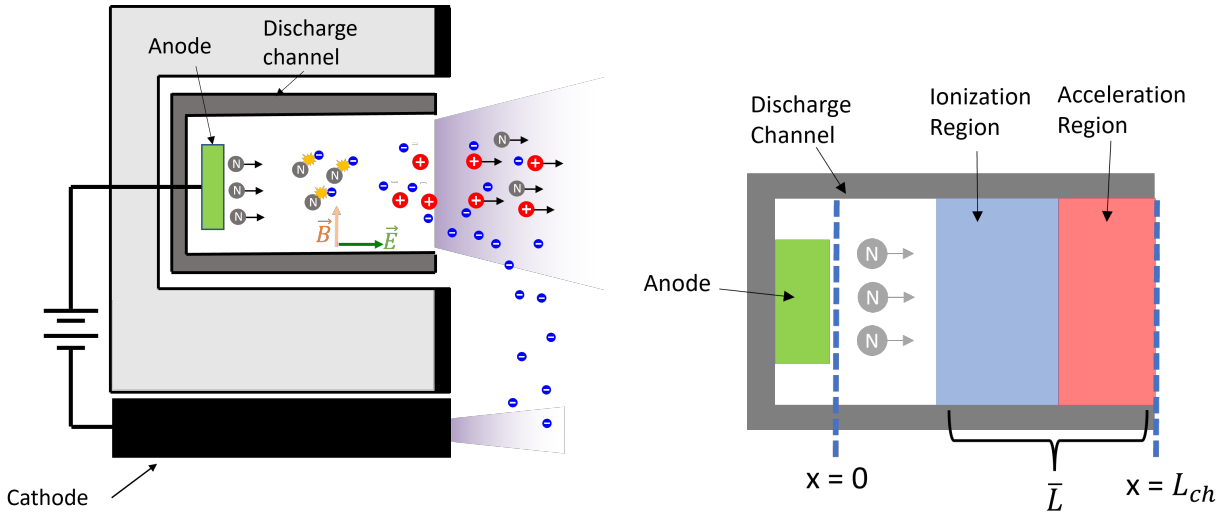

(a) (b)

Figure 1: a) Hall thruster cross section and operation. b) Zoomed in view of the discharge channel region.

negative cathode. The hollow cathode thermionically emits electrons that are impeded on their path to the anode by the radial magnetic field. These electrons gyrate around field lines and drift azumithally due to crossed perpendicular electric and magnetic fields. The drifting electrons collide with and ionize the majority of neutral gas in the "ionization region", shown in Fig. 1 (b). These newly created ions remain unmagnetized due to their large mass and are accelerated downstream by the potential drop to produce thrust. This region of large potential decrease is referred to as the "acceleration region".

In a modern Hall thruster, the majority of the input neutrals are ionized. This process lends itself to the definition of the mass utilization, or fraction of ionized input propellant:

$$\eta_m = 1 - \frac{\dot{m}_n(L_{ch})}{\dot{m}_n(0)} = 1 - \frac{n_n(L_{ch})}{n_n(0)} \tag{1}$$

In this expression, $\dot{m}_n(0)$ is the neutral mass flow rate at the anode (0), and $\dot{m}_n(L_{ch})$ is the neutral mass flow rate at the channel exit (L_{ch}). We have assumed here that the neutral thermal velocity, channel area, and average neutral mass remain constant along the channel length so that the ratio of mass flow rates can be written in terms of number density n_n. Intuitively, this equation indicates that if no neutrals remain at the channel exit (all are ionized), the mass utilization is unity.

To relate the mass utilization to key aspects of the thruster operation, we motivate an analytical expression for the ratio of the exit and inlet neutral densities. We find this from a consideration of the 1-D, steady-state, neutral continuity equation:

$$v_n \frac{dn_n}{dx} = -n_n n_e k_{iz}(T_e), \tag{2}$$

where v_n is the neutral velocity, n_e is the electron number density, and $k_{iz}(T_e)$ is the total ionization rate coefficient averaged over a Maxwellian electron population with temperature T_e. We define the neutral

thermal velocity as $v_n = \sqrt{kT_n/m}$, where T_n is temperature, k is the Boltzmann constant, and m is the neutral mass. Next, we integrate this expression from the anode (x = 0) to the end of the channel (x = L_{ch}) and combine the result with Eq. 1 to yield

$$\eta_m = 1 - \exp\left[-\frac{\langle n_e\rangle\langle k_{iz}(T_e)\rangle}{v_n}\bar{L}\right], \tag{3}$$

where we have replaced the channel length L_{ch} with a characteristic length $\bar{L}$, and denote average quantities with $\langle\rangle$. Physically $\bar{L}$ represents the combined width of the ionization (L_{iz}) and acceleration region (L_{acc}) and does not necessarily equal the full channel length. Since the important Hall thruster physics that dictate propellant ionization primarily occur in these two regions, we define an average plasma density and electron temperature (ionization rate) across this zone. Eq. 3 highlights the key parameters that impact the mass utilization efficiency. Notably, longer characteristic lengths, denser plasma's, and higher ionization rates promote a larger ionization fraction while faster thermal velocities lower ionization.

Now that we have introduced our mass utilization formulation in terms of plasma properties, we next attempt to relate these to global properties of the thruster operation e.g. discharge voltage and current. To that end, for the density, we first consider a generalized ohm's law where we neglect the pressure contributions:

$$j_e = E\sigma = E\frac{m_e n_e \nu_c}{B^2}, \tag{4}$$

where j_e is the electron current density, E is the electric field, σ is the conductivity perpendicular to the magnetic field B, m_e is the electron mass, and ν_c is the electron collision frequency. We assume that the collision frequency is Bohm-like, and scales as

$$\nu_c = \alpha\omega_e, \tag{5}$$

where $\omega_e = qB/m_e$ is the electron cyclotron frequency, and α is a constant on the order $10^{-2} - 10^{-3}$.[7,8] We estimate the electron current density as

$$j_e = j_D(1 - \eta_b), \tag{6}$$

where j_D is the discharge current density. η_b is the beam utilization efficiency defined as

$$\eta_b = \frac{j_b}{j_D}, \tag{7}$$

where j_b is the ion current density. In this study, one of the main parameters we vary is the discharge current density, which we estimate as $j_D = I_D/A_{ch}$. We approximate the electric field in Eq. 4 as the ratio of the voltage drop in the channel V_{ch} to length of the acceleration region L_{acc}. We formulate the voltage drop in the channel V_{ch} as

$$V_{ch} = V_D - V_{cc}, \tag{8}$$

where V_D is the discharge voltage and V_{cc} is the cathode coupling voltage. Physically, Eq. 8 indicates that the potential drop in the channel is reduced by the voltage needed to extract electrons from the cathode V_{cc}. Subject to this definition, we can then employ Eqs. 3–8 to write the mass utilization as

$$\eta_m = 1 - \exp(-\frac{\bar{L}}{\lambda_i}), \tag{9}$$

where we have introduced the parameter λ_i defined as

$$\lambda_i = \sqrt{\frac{T_n k_b}{m_i}}\frac{(V_D - V_{cc})\alpha q}{L_{acc}B(1-\eta_b)\langle k_{iz}(T_e)\rangle j_D}. \tag{10}$$

Physically, λ_i represents the mean free path for ionization, and according to this simplified theory will universally predict the mass utilization efficiency at all operating conditions on each gas. Indeed, a key feature of this result is that provided the scaling length, $\bar{L}$, is approximately constant, the mass utilization of any gas or operating condition, when expressed in terms of this effective ionization length, should collapse onto a single curve. To evaluate this in practice, we consider in the following section experimental data generated parametrically over four different gases and a range of operating conditions.

III. Experimental Setup

In this section, we outline the experimental setup used to generate the mass utilization data we leveraged in this investigation. We outline the configuration and setup with descriptions of the thruster configuration, operating conditions, facility, and diagnostics.

A. Thruster Configuration

In this campaign, we utilized a modified version of the H9 Hall thruster. This device is a 9 kW class Hall thruster previously developed through a collaboration of the Jet Propulsion Laboratory, the University of Michigan, and the Air Force Research Laboratory.[9,10] This thruster employs a magnetically shielded topography where the magnetic field is tailored to reduce erosion of the channel walls[11,12]. The H9 has been extensively characterized on both xenon and krypton and shares design features with the advanced electric propulsion system (AEPS).

The version of the H9 we utilized in this work is based on the modified version described in Ref. 13. Key elements include a graphite discharge chamber, water cooled magnetic bobbins, and a centrally mounted hollow Lab6 cathode.

Electrically, the thruster body was grounded for most experimental configurations with a few exceptions where the body was electrically tied to the cathode. We believe this configuration difference had a minimal impact on the results given the past studies of ref. 14. The magnetic field magnitude was tailored to be consistent with the previous parametric study on the H9.[6]

B. Operating conditions

Table 1 shows the range of operating conditions and propellants for which we experimentally measure the mass utilization. We note in this table as well the origin of the data. For both xenon and krypton, we leveraged an existing dataset from the work of Su et. al. in which the mass utilization of krypton and xenon were experimentally characterized as a function of operating condition.[6] We note here that we have re-processed the probe data gathered in Ref. 6 to reflect the updated E×B analysis procedures detailed in Sec. IV A1.

For this study, we expanded on the operating envelope of previous work to include parametric studies on both argon and nitrogen across a range of discharge current densities. On nitrogen, we kept the discharge voltage fixed at 300 V and on argon we operated at both 200 V and 300 V. At each new condition, we set the discharge voltage, and varied the mass flow rate to both the anode and cathode until the target discharge current density was met. We operated the cathode at a constant 7% particle flow fraction of the anode. We used krypton gas for the cathode when the thruster was operating on nitrogen to avoid poisoning.[15] Once the mean discharge current reached a constant value, we utilized a suite of far field probes to experimentally infer the mass utilization.

Gas	Discharge Voltage	Anode Flow Rate Range	Data Source
Argon	300	1–6.43x	This Work
Argon	200	1–5.95x	This Work
Nitrogen	300	1–4.78x	This Work
Xenon	300	1–4.48x	Ref. 6
Krypton	300	1–5.99x	Ref. 6

Table 1: List of the discharge voltages and normalized flow rate range for each gas.

C. Facility

In this work as well as for the data extracted from Su et. al.[6],we operated the thruster in the Alec D. Gallimore Large Vacuum Test facility at the University of Michigan. Fig. 2 shows a top down view of the experimental setup. This chamber is 6 m x 9 m and utilizes 12 shrouded TMI-1200i and 5 nude cryosails. The cryosails were specifically designed to pump xenon and krypton at 35-40 K, and therefore are too warm to

effectively capture argon or nitrogen.[16] As a result, we only utilized the 12 shrouded pumps for this work. To measure background pressure, we utilized a wall mounted IGM401 "Hornet" hot cathode ionization gauge. As shown in Fig. 2, during operation, we oriented the thruster plume downstream facing the far-field probes. The Faraday probe was $\sim 10\ D_T$ and the E×B probe and Langmuir probe were 12.5 D_T downstream.

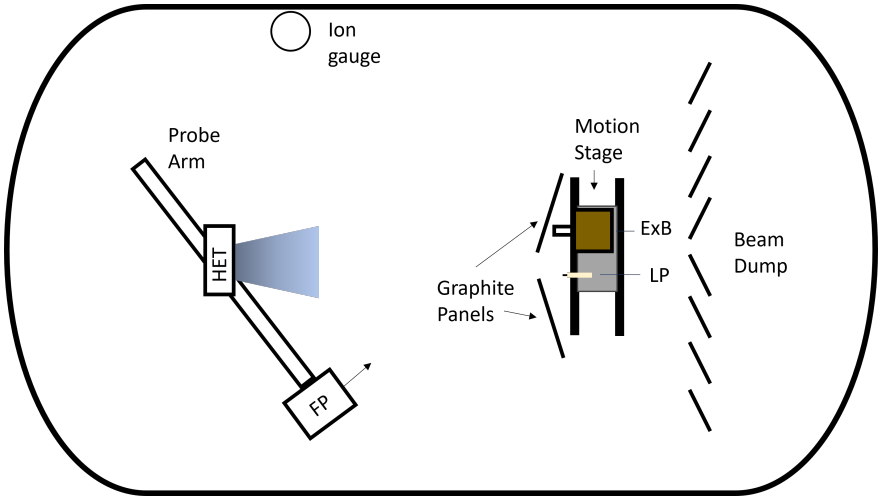

Figure 2: Top down view of the experimental setup in LVTF. Included are the positions of the thruster, Faraday probe on the azimuthal arm, wall mounted ion gauge, and E×B/Langmuir Probe on a far field motion stage.

D. Diagnostics

To experimentally infer the mass utilization and provide estimates for key quantities of interest in our mass utilization model, we utilized a far field probe suite consisting of a E×B probe, Faraday Probe, and Langmuir Probe. Table 2 provides a summary of the probes and inferred quantities. The Faraday probe was mounted on an azimuthally swept probe arm at a constant radius of $R = 10D_T$, where D_T is the thruster diameter. The arm was swept from 0-180° and back, where 90° is defined as the thruster centerline. The Langmuir and E×B probes provided a single-point probe trace on centerline at $R = 12.5D_T$.

The guarded, molybdenum Faraday probe we employed to estimate the ion beam current was 2.38 cm in diameter. Both the collector and guard ring were biased to -30 V to collect ion saturation current. The E×B probe, which measures current fractions (Ω) in the beam, imposes a magnetic field of 0.16 T between two electrodes spaced 0.97 cm apart. The E×B probe has an entrance collimator with an aperture of 1.6 mm and a length of 7.5 cm, and an exit collimator that is 15 cm long. We swept the plate potential from 0-150 V to capture ion species of different velocities. We utilized a 1 mm diameter by 4 mm length cylindrical Langmuir probe to infer the plasma potential, V_p. The plasma potential is used to calculate the cathode coupling voltage V_{cc}. We follow the recommended Langmuir probe analysis procedure outlined ref. 17 to estimate this quantity.

Probe	Measured Quantity	Inferred Property
E×B Probe	Ω_s	η_m
Faraday Probe	I_b	η_b and η_m
Langmuir Probe	V_p	V_{cc}

Table 2: List of the far field probes and their measured quantities.

IV. Analysis

In this section, we discuss the analysis techniques used to infer the key plume properties needed to experimentally estimate the mass utilization efficiency. We then outline our process for regressing the proposed model for mass utilization.

A. Experimentally Measuring Mass Utilization

We can use far field plume measured quantities to experimentally estimate the mass utilization efficiency as

$$\eta_m = \frac{\dot{m}_i}{\dot{m}_a} = \frac{I_b}{\dot{m}_a} \sum \frac{\Omega_s m_s}{q_s}, \tag{11}$$

where $\dot{m}_a$ is the anode mass flow rate (denoted $\dot{m}_n(0)$ in Eq. 1) and $\dot{m}_i$ is the ion mass flow rate. Eq. 11 highlights that if we can measure the total ion beam current and the fraction of current carried by each species, we can estimate the ion mass flow rate and thus mass utilization efficiency. In the following sections, we outline the analysis process to estimate and quantify the uncertainty of these quantities.

1. *Ion Beam Current*

We relate the beam current I_b to ion current density measured in the far field with the relationship

$$I_b = 2\pi R^2 \int_0^{\pi/2} j_i(\theta) \cos\theta \; d\theta., \tag{12}$$

where $j_i(\theta)$ is the ion current density measured at an angle θ in the far field plume. An example Faraday trace of the thruster operating on argon is shown in Fig. 3. We can relate the Faraday probe ion saturation current measurement I_{FP} to current density according to the following equation:

$$j_i(\theta) = \frac{I_{FP}}{A_C + \kappa_G} \kappa_{SEE}. \tag{13}$$

Here, A_c is the collector area, κ_G is a correction factor for additional ions collected in the gap between the collector and guard ring, and κ_{SEE} is a correction factor due to ion impact secondary electron emission.[18] The formulas for each of these correction factors are listed in the appendix. The values of the SEE coefficients are taken from Refs. 19–21.

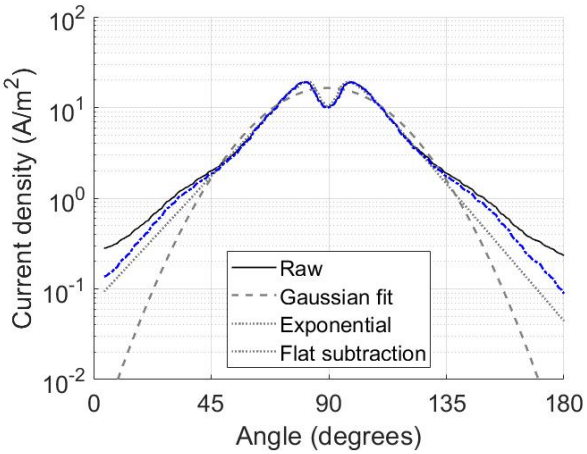

Figure 3: Ion current density profile operating on argon at a discharge voltage of 300 V with the different charge exchange correction methods plotted.

Before integrating the corrected Faraday probe trace for use in Eq. 13, we perform a series of deconvolution methods, shown in Fig. 3, to account for charge exchange of the main beam with the background neutrals. In short, each of these methods is intended to correct for the additional current density observed in

the wings of the trace due to large angle CEX scattering. The three methods used to account for CEX were a Guassian fit[18], exponential fit[22], and a flat subtraction[23]. We parse each segment of the Faraday probe sweep 0–90°, 90–180° and back into four unique estimates of the beam current. We perform the CEX fits to each of these four traces, integrate the current density trace, and then average the results for our estimate of the beam current. We estimate the uncertainty as twice the standard deviation of the data set.

2. *Charge fractions*

We utilize the trace generated by the E×B probe to estimate the current carried by each species in the beam. The E×B probe selectively filters ions of a given velocity. Since ions with different charge states or masses will be accelerated to different speeds $v_s \approx \sqrt{\frac{2q_s V_d}{m_s}}$, we can identify the distribution of each species in the spectra. Once we learn the underlying distributions $f_s(V)$ we use the integral equations outlined in Ref. 24 to calculate the charge fractions as

$$\Omega_s = \frac{\int \frac{q_s}{m_s} f_s(V_p)/V_p^2 dV_p}{\sum \int \frac{q_k}{m_k} f_k(V_p)/V_p^2 dV_p}, \tag{14}$$

where V_p is the plate voltage difference. Fig. 4 shows an example E×B trace at two operating conditions on xenon from Ref. 6.

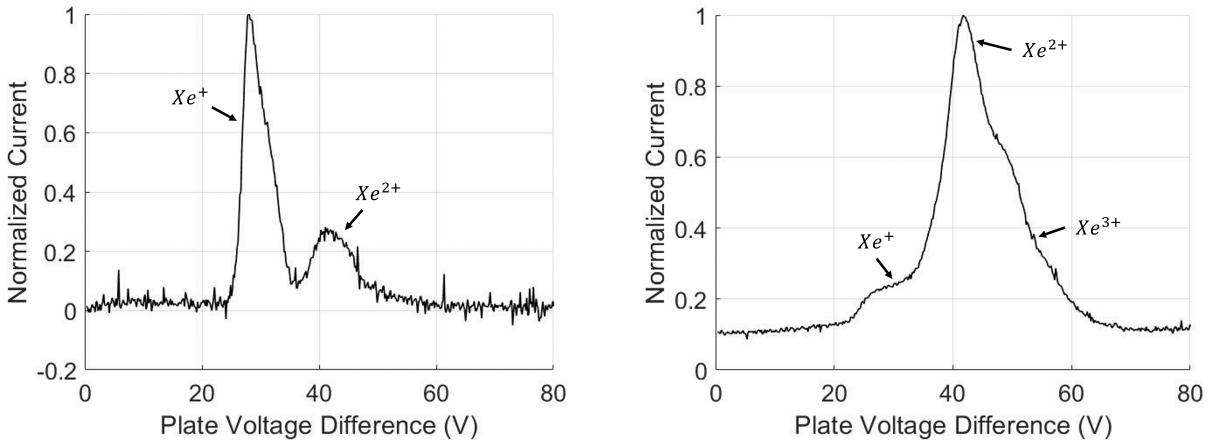

Figure 4: E×B spectra of the thruster operating on xenon at a) $V_d = 300$ V, $I_d = 15$ A and b)$V_d = 300$ V, $I_d = 100$ A.

Notably, in Fig. 4a we see two distinct peaks corresponding to each ion charge state for xenon. Generally, the fitting process, as detailed by Huang et al.[24], is to assume a form of the ion velocity distribution and fit to each peak sequentially. This fitting method has historically performed well for estimating the charge fractions when each peak is distinct, but it does not provide an estimate of the fit uncertainty. Quantifying the uncertainty in the current fractions is especially important when the distributions overlap as changes in the fitting windows of a few volts or the order in which peaks are fit can result in >10% changes in the magnitude of the resulting current fractions.

As an attempt to more rigorously account for uncertainty, we utilize Bayesian inference to fit to all the peaks simultaneously. In Bayesian inference, we update our prior belief in the parameters θ, after seeing data d through Bayes' rule written as

$$P(\theta|d) \propto P(d|\theta)P(\theta), \tag{15}$$

where $P(\theta)$ is our prior distribution over the parameters, $P(d|\theta)$ is the likelihood distribution, and $P(\theta|d)$ is the posterior distribution. Assuming the data has a Gaussian noise γ, the likelihood is distributed normally as

$$p(d|\theta) \sim N(g(d,\theta),\gamma), \tag{16}$$

where $g(d,\theta)$ is our model for the E×B fitting. In this initial investigation, we assume each unique ion population in the plume is normally distributed. Therefore, our model takes the form

$$g(d,\theta) = \sum A_s \exp\left(\frac{(x-\mu_s)^2}{\sigma_s^2}\right) \tag{17}$$

where our parameters θ are the mean μ_s, width σ_s, and prominence A_s of the distribution for each species "s". For the parameters A_s and σ_s, we assume uniform priors. We assume each mean μ_s of our model is distributed normally and centered the plate voltage corresponding to the velocity of species "s". Assuming the electric field is constant between the plates, we can write the expected plate voltage corresponding to each species as

$$V_{p(s)} = B_{ExB} w \left(\frac{2q_s(V_d - V_{cc})}{m_s}\right)^{1/2}, \tag{18}$$

where $V_{p(s)}$ is the plate voltage difference for species "s", B_{ExB} is the magnetic field, and w is width between the plates. As a first estimate, in this formulation, we assume that the ions fall through a potential drop equal to the difference between the discharge voltage and cathode coupling voltage. Since our model is non-linear, we cannot easily solve Bayes' rule for the posterior distribution. Therefore, we utilize Markov-Chain Monte Carlo to sample from the un-normalized posterior distribution defined on the right side of Eq. 16. We then take the mean of the resulting distribution to be the best estimate of each parameter. In Fig. 5, we show an example fit to the E×B spectra of Fig. 4b, where the blue bounds represent 95 % confidence intervals.

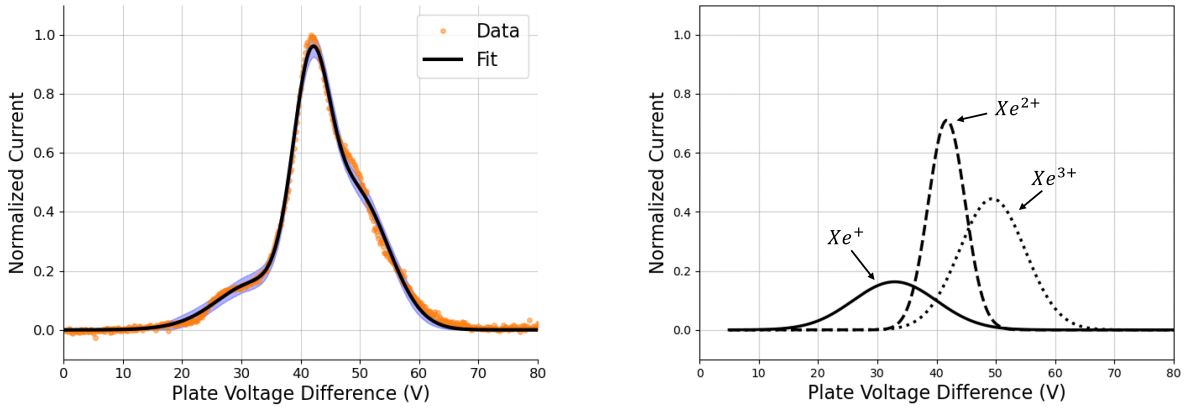

(a) (b)

Figure 5: a) The E×B spectra fit with 95 % confidence intervals plotted in blue, and b) the underlying distributions of each species.

Evidently, we see that the model fits to the data well. We calculate the current fractions with Eq. 14 for each sample drawn from our posterior distribution. We then take the sample mean and standard deviation of the resulting data set to be our best estimate of the current fractions and uncertainties. We note here that since we utilized this new fitting method to calculate current fractions, the resulting mass utilization for xenon and krypton is $\sim$ 2-5 % different than than presented in Ref. 6. We compare estimated current fractions from both methods in Sec. VI.

Due to charge exchange of the thruster plume with background neutrals, the current fractions measured by the E×B probe are different than those leaving the thruster. To correct for charge exchange, we follow the procedures outlined in Ref. 24. For argon and nitrogen, we utilize charge exchange cross section data from Ref. 25. The uncertainty in the charge exchange correction stems largely from error in the background pressure estimate which is $\sim$ 20% for the ionization gauge we utilized. We estimate this CEX correction

uncertainty following analysis of Ref. 24, and combine the result in quadrature with the uncertainty in the raw current fractions.

B. Model Assumptions and Calibration

In this section, we describe the key model assumptions and calibration procedures we employed in this analysis. First, we outline our assumptions for each parameter in the ionization mean free path (Eq. 10).

- **Constant beam utilization efficiency** η_b: The beam utilization, inferred from the Faraday trace, has been observed to vary little ($\sim$ 5-10 %) between gases and operating conditions in both this work and Ref. 6. We average η_b across all operating conditions and gases to estimate it as $\eta_b = 0.75$.
- **Constant cathode coupling voltage** V_{cc}: The voltage needed to extract cathode electrons, or cathode coupling voltage, is directly measured with the cathode to ground voltage and plasma potential: $V_{cc} = V_{c2g} - V_p$. Experimentally, we observe this quantity to vary by < 5 V across all operating conditions. We average V_{cc} across all operating conditions and gases to estimate it as 25 V.
- **Constant length of acceleration region** L_{acc}: The length of the acceleration region, which determines the electric field in ohm's law, is a non-linear function of parameters like magnetic field shape/strength, discharge voltage, and background pressure, which makes it difficult to determine *a-priori*.[26,27] Non-invasive measurements of this acceleration region show that the width is typically $\sim$ 3-7 mm across a range of discharge voltages, operating pressures, and gases.[26–28] Therefore, in this analysis, we make the strong assumption that it is a constant 5 mm.
- **Electron temperature scales with discharge voltage**: Electrons gain energy through Ohmic heating, which is proportional to the applied discharge voltage. We approximate this electron temperature scaling as $T_e = 0.1V_d$.[1,29]
- **Neutral thermal velocity scales per Eq. 19**: We assume the neutral population moves at the thermal velocity determined by the anode temperature. As outlined in Eq. 19, we assume radiation dominates and that the anode temperature increases with thruster discharge power.
- **Electron collision frequency is constant and bohm-like**: Per Eq. 5, we assume the electron collision frequency is constant and scales with the cyclotron frequency scaled by a constant α. To estimate α, which physically represents the inverse Hall parameter, we utilize direct experimental measurements of the H9 operating on krypton presented in Ref. 8, which show $\alpha \approx 1E-2$.

We utilize the electron temperature in conjunction with the total ionization cross section for each species to determine the ionization rate coefficients $k_{iz} = \langle v_e(T_e)\sigma_{iz}\rangle$. We plot the ionization rate coefficients for each gas in Fig. 6.

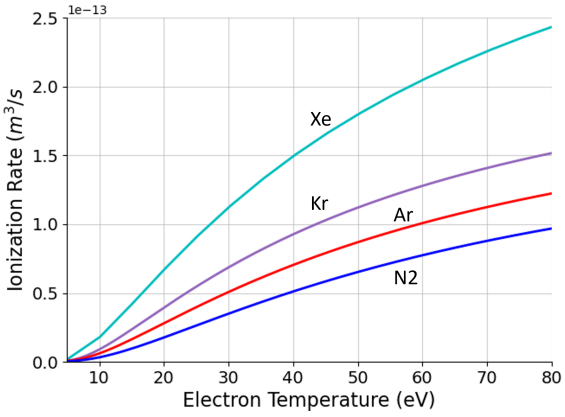

Figure 6: Ionization rate coefficient k_{iz} for xenon, krypton, argon, and nitrogen as a function of electron temperature.

Evidently, we see that at a given electron temperature, xenon has the largest ionization rate, followed by krypton, argon and then nitrogen. The ionization rate monotonically increases as the electrons gain more energy (higher T_e). In this analysis, we allow the neutral temperature T_n to vary across operating conditions. This is physically motivated since we expect the neutral particles to thermalize with a higher temperature anode as the discharge power increases. As a first approximation of this scaling, we make the strong assumption that radiation dominates, and formulate the neutral temperature as

$$T_n = T_{ref}(\frac{P}{P_{ref}})^{\frac{1}{4}}, \tag{19}$$

where we define the reference temperature T_{ref} and power P_{ref} to be 400 C and 4.5 kW. These values correspond to our best estimate of the anode temperature while operating on xenon at a discharge voltage of 300 V and current of 15 A. We summarize the model input parameters in Tab. 3.

Parameter	Value
T_e	$0.1V_d$ eV
η_b	0.75
V_{cc}	25 V
α	1E-2
L_{cc}	5 mm
T_{ref}	400 C
P_{ref}	4.5 kW
B	$B_{r_{max}}$

Table 3: Key model assumptions of plasma parameters.

Since the combined length of the ionization and acceleration region, termed the characteristic length $\bar{L}$, is difficult to estimate, we learn it from the data with Bayesian inference. As outlined in Sec. IVA., Bayesian inference updates our prior belief in parameters after seeing data. In this case, our data is the experimentally measured mass utilization. We impose a uniform prior of the form U(0,1.25L_{ch}), which physically means that $\bar{L}$ is equally likely to take any value from 0 to 1.25L_{ch}. Since the peak magnetic field, and thus acceleration process happens downstream of the thruster exit plane in magnetically shielded Hall thrusters, we explicitly allow for lengths longer than the baseline channel.

V. Results

Here we compare the results of our mass utilization model to the experimental data. As outlined in Sec. IV, we utilize Markov-Chain Monte Carlo to learn a characteristic length $\bar{L}$ for all species. In Fig. 7 we compare our model predictions to experimental data as a function of the normalized inverse ionization mean free path $1/\bar{\lambda}_i$. We normalize to the largest inverse ionization mean free path in our data set. In Fig. 7, the shaded red region is the 95% confidence intervals resulting from the posterior distribution of the learned parameter $\bar{L}$.

The experimentally inferred mass utilization for each gas generally improves as the ionization mean free path decreases. The increase in ionization efficiency is non-linear and plateaus to near unity. Physically, a smaller λ_i leads to enhanced ionization until all input propellant is ionized. For each gas species, we see that the uncertainty in mass utilization increases with decreasing ionization mean free path. This can be largely attributed to uncertainty in the fraction of current (Ω_s) carried multiply charged species at increased currents. Per the discussion in Ref. 6, higher discharge currents and therefore smaller mean free paths per Eq. 10, translates to higher production rates of multi-charged ions. As a result, our ability to identify the individual current fractions for each species suffers, resulting in a higher mass utilization uncertainty. We note here as well that the enhanced current fraction uncertainty may be a contributing factor to the results that exhibit mass utilization higher than unity.

In Fig. 7, we see that our mass utilization model (black line) follows the same non-linear increase to unity as the experimental data. This is a direct result of Eq. 9, which shows that mass utilization monotonically increases with decreasing λ_i until all the inpu propellant is ionized. In general, we see that the uncertainty in

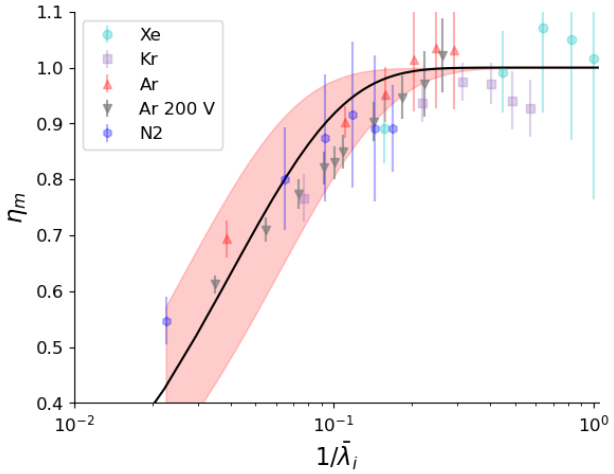

Figure 7: Experimental data and mass utilization model plotted against the normalized inverse ionization mean free path. The 95% confidence intervals of the learned parameter $\bar{L}$ are plotted in red.

the experimental mass utilization for all data points falls within the 95 % confidence intervals of the model prediction. This indicates that our model follows the same trends as the data which may lend support to our underlying assumptions.

The 95% confidence intervals of the model stem from the posterior distribution of the parameter $\bar{L}$, the characteristic length. In Fig. 8, we present a histogram of samples drawn from the posterior distribution of $\bar{L}$. In this plot, we have normalized $\bar{L}$ to the thruster channel length L_{ch}

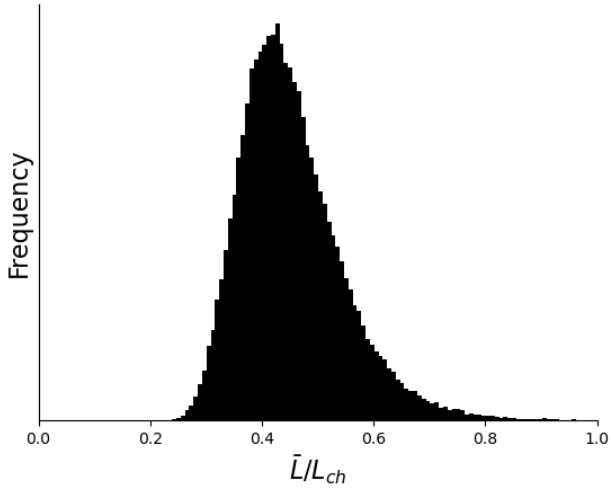

Figure 8: Histogram of samples drawn from the posterior distribution of $\bar{L}$ normalized to the thruster channel length L_{ch}

We see that the histogram of samples in Fig. 8 appears to take the form of a skewed exponential distribution (Gamma, Skew-normal) centered at $\bar{L}/L_{ch} = 0.45$. The 95% confidence intervals are CI[0.31,0.68]. Since $\bar{L}$ represents the combined width of the ionization and acceleration region, negative values are non-physical. As a result, we see a skew in the distribution towards larger $\bar{L}$. The breadth of the distribution, which represents our uncertainty in the characteristic length, is directly related to the uncertainty in the mass utilization data. The mean value of this distribution ($\bar{L}/L_{ch} = 0.45$.), which represents our best estimate of $\bar{L}$, is qualitatively similar to that found in calibrated high fidelity simulations of this thruster.[28] Indeed, in both cases, the combined width of the ionization and acceleration zone is $\sim 1/2$ of the channel length. This agreement indicates that our simple model is capturing some of the underlying physics driving the mass

utilization efficiency.

VI. Discussion

In this section, we discuss the notable results of this analysis. This includes a description of the key limitations of this model, trends in predictions with discharge voltage, and uncertainty in inferring current fractions.

A. Model Limitations

While our model for the mass utilization does capture the experimental data, it has some key limitations, which we discuss here. First, since the model is 0-D, it cannot capture the non-linear changes along the discharge channel in electron temperature and plasma density typically exhibited in detailed thruster simulations.[28,30] Since the ionization rate (k_{iz}) is a non-linear function of the electron temperature for each species (Fig. 6), assigning a single k_{iz} for each gas is a inherent strong assumption of this formulation.

Another key assumption we made in our model is that the ratio of mass flow rates at the anode and channel exit could be re-written in terms of the ratio of number densities at the two locations (Eq. 1). While this is valid for the noble gases tested, it may not a good approximation for gases that can dissociate like nitrogen. More accurately, the mass utilization for nitrogen should be written as

$$\eta_m = 1 - \frac{\dot{m}_n(L_{ch})}{\dot{m}_n(0)} = 1 - \frac{n_{N_2}(L_{ch})m_{N_2}v_{N_2} + n_N(L_{ch})m_N v_N}{n_{N_2}(0)m_{N_2}v_{N_2}}, \tag{20}$$

where we have defined species specifics quantities with the subscripts N and N_2. While the formulation of Eq. 20 is more accurate, it is difficult to use in practice. This is because the neutral continuity equation for monotonic and diatomic nitrogen are coupled to each other, and cannot be easily integrated. Therefore, to keep the simplicity of the model, we ignored the monotonic species which may have effected the accuracy of the predictions. Since monotonic nitrogen has a faster thermal speed due to its lighter mass, neglecting this species would lead to an over-prediction of the mass utilization efficiency. This explanation could be one reason why at the shortest λ_i conditions for nitrogen, the model over-predicts the mass utilization. This is in contrast to the longer λ_i conditions for nitrogen where the model captures the data more accurately.

Lastly, we note that there are some parameters in λ_i that we do not vary significantly in this study. Namely, we do do not alter the magnetic field strength, and we investigate a narrow range of discharge voltages (200-300 V). Furthermore, we gather data on a single thruster in one configuration for all conditions tested, which keeps other parameters like the beam utilization and cathode coupling voltage relatively constant. Therefore, our conclusion that the model captures the experimental mass utilization data could be limited to the ranges tested in this work until more experimental data is gathered. To test the extensibility of this model for one of these parameters, we look its scaling with discharge voltage in Sec. VI B.

B. Scaling of η_m with Discharge Voltage

In this study, we demonstrated that the model accurately captures the experimental data over the range of discharge voltages tested. In this section, we extend the model by parametrically varying the discharge voltage beyond the scope of the experimental data to see how the mass utilization predictions scale. We fix the discharge current to 15 A for this analysis and utilize the same assumptions described Sec. IV for the remaining parameters in λ_i. In Fig. 9a, we plot the mass utilization prediction with discharge voltage for xenon, krypton, argon, and nitrogen.

The mass utilization prediction for each species with discharge voltage follows a similar non-monotonic trend. We first see an increase in mass utilization with discharge voltage followed by a decrease. This non-monotonic behavior has been observed previously on many different Hall thrusters operating on xenon with increasing discharge voltage at a fixed discharge current or mass flow rate.[22,23,31] This trend in the mass utilization can be explained by our formulation of the ionization mean free path ,Eq. 10, which we re-write here in terms of parameters that vary with discharge voltage as

$$\lambda_i \propto \frac{V_d\sqrt{T_n}}{k_{iz}(T_e)},\ T_e = 0.1V_d. \tag{21}$$

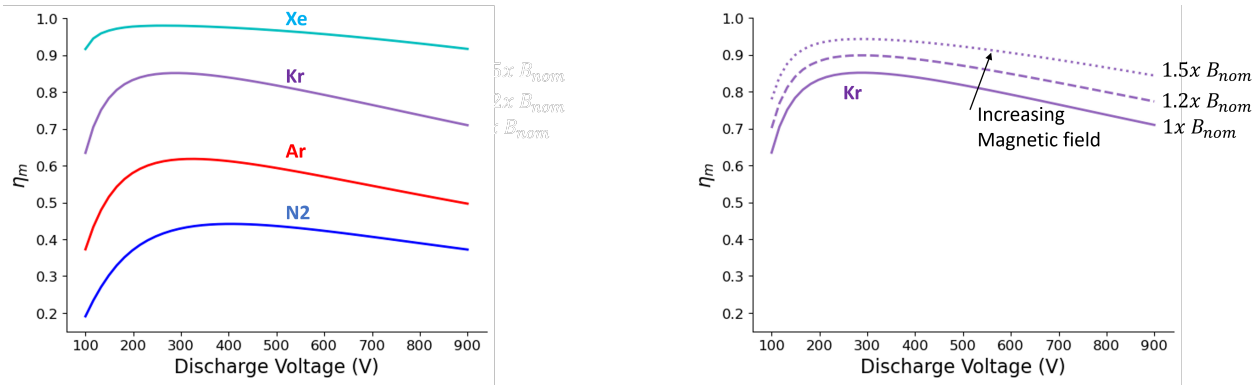

(a) (b)

Figure 9: (a) Model mass utilization efficiency predictions as function of discharge voltage for different gas species and (b) magnetic field strength.

Notably, in this formulation we can see that the ionization mean free path is a balance between the discharge voltage and neutral temperature against the ionization rate. A higher discharge voltage leads to more electron cross field transport and thus lower channel plasma density. The neutral temperature grows with discharge voltage as well due to enhanced power deposition to the anode. These two effects serve to increase the ionization mean free path and decrease ionization. This is balanced by the ionization rate, which increases monotonically with discharge voltage (hotter T_e). Looking at Fig. 6, we see that there is a sharp increase in the ionization rate for all gases between 10 and 20 eV, which corresponds in Fig. 9 to an rise in mass utilization at lower voltages (100-200 V). At higher T_e/V_d, the ionization rate grows slower than the discharge voltage and neutral thermal temperature, leading to a decrease in the mass utilization.

Per Eq. 10, one free parameter that can be utilized to mitigate the decrease in mass utilization at large discharge voltages is the magnetic field strength. In Fig. 9b, we see that the mass utilization increases with the applied magnetic field. Physically, larger magnetic field strengths better confine electrons in the channel, resulting in higher electron densities and propellant utilization. The scaling of the magnetic field strength with discharge voltage for optimal thruster efficiency has been demonstrated both experimentally and theoretically in previous work.[29,32,33]

The fact that our model captures observed experimental trends in both discharge voltage and magnetic field strength (Refs. 22,23,31,32), at least qualitatively, suggests that our model captures some of the underlying physics driving mass utilization with these parameters. With that being said, experimental data at higher discharge voltages and different magnetic field strengths is needed for verification.

C. Uncertainty in Inferring Current Fractions

One of the primary sources of uncertainty in the inferred mass utilization is estimates of the current carried by each species. As an example, for the same input mass flow rate and beam current, a beam comprised of singly charged ions would have twice the mass utilization efficiency of a beam comprised of doubly charged ions. As we detailed in Sec. IVB., overlapping species distributions on the ExB spectra can make identifying the current fractions and the associated uncertainty difficult. Indeed, sequentially fitting to each peak and subtracting can lead to large variations in the resulting current fractions that depend on the fitting window and order in which the peaks are fit. Therefore, we proposed a new method outlined in Sec. IVB. where we fit to all peaks of the E×B spectra at the same time using Bayesian inference. Here we compare the results of this new fitting method to the sequential method utilized in Ref. 6. We utilize the xenon E×B data here to present a case with significant distribution overlap. We plot the resulting current fractions calculated from the spectra as a function of the normalized inverse ionization mean free path $1/\bar{\lambda}_i$ in Fig. 10.

In general, we see that current fractions predicted by each method follow the same trends. Notably, when the peaks are more distinct (large λ_i, Fig. 4a), the new fitting method agrees well with the sequential method. As λ_i decreases and the species distributions become more convoluted (Fig. 4b), the two methods begin to diverge. This discrepancy is an expected result given the difficulty in determining the current fractions

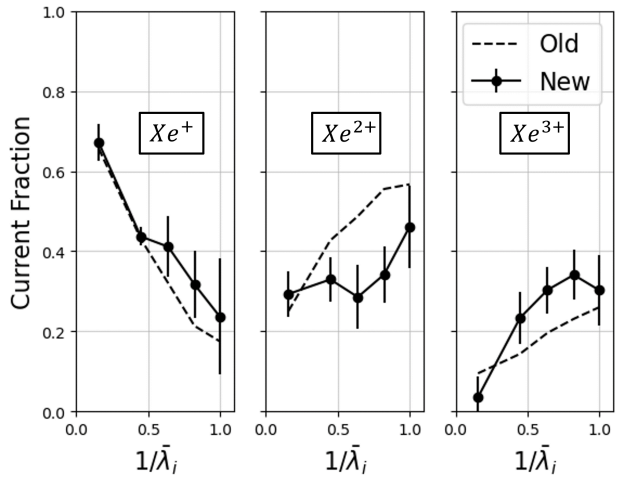

Figure 10: Comparison of current fractions calculated with the sequential fitting method termed "old", and the Bayesian fitting method termed "new" for xenon as a function of the normalized inverse ionization mean free path $1/\bar{\lambda}_i$. The sequential fitting method data is reproduced from Ref. 6.

at these conditions. While we do not claim that the Bayesian fitting method gives a better estimate of the "true" current fractions, we do believe it more accurately captures the uncertainty. This trait can be seen in the uncertainty bounds of Fig. 10, where the bound magnitude grows as the distributions become more convoluted. Therefore, this new fitting method could be a useful tool to help bound the current fraction predictions when species overlap.

VII. Conclusion

The mass utilization is a key figure of merit for Hall thrusters that historically suffers for non-conventional, more difficult to ionize gases. In order to elucidate the underlying physics that govern mass utilization, we have proposed in this work a first principles scaling law for the physical processes that drive ionization on disparate gases. The quasi-0D model was derived by integrating the neutral continuity equation along the length of the thruster channel. The result is a simple scaling law that relates the combined with of the Hall thruster ionization and acceleration region, termed the characteristic length, to the ionization mean free path for each operating condition. To validate the model, we collected mass utilization data on a magnetically shielded Hall thruster operating on various propellants. This includes data from previous campaigns on xenon and krypton, and new data collected on argon and nitrogen. On each propellant, we parametrically varied the ionization mean free path and inferred the mass utilization with a suite of far field probes. To help analyze overlapping species distributions seen in the E×B spectra, we proposed a Bayesian fitting methodology. While the quality of fit was similar to heritage E×B fitting methods, we were able to better capture uncertainty in the species current fractions that propagate into a mass utilization prediction. The results indicate that with a learned characteristic length for the entire data set, the model accurately captures the trends in mass utilization as a function of the ionization mean free path for each gas. This suggests that our model may be capturing some of the underlying physics that drive ionization in magnetically shielded Hall thrusters. To further test our formulation, we explored the model predictions outside the range of experimental data. We demonstrated that the model is consistent with the observed non-monotonic scaling of mass utilization with discharge voltage seen in other Hall thrusters. Given the accuracy of the scaling law over a wide range of experimental data, this model could be a beneficial tool for understanding the driving processes that influence mass utilization of thrusters operating on disparate propellants.

Appendix

We correct the Faraday probe trace for extra current collected between the guard ring and collector with the correction factor κ_G defined as

$$\kappa_G = \pi(R_{GR}^2 - R_C^2)\frac{2\pi R_c h_c}{2\pi R_c h_c + 2\pi R_{GR} h_{GR}}, \tag{22}$$

where R_c, h_c, R_{GR}, and h_{GR} are the heights and radii of the collector and guard ring. Additionally, a correction factor must be applied to account for secondary electron emission from the probe due to ion impact. This factor, κ_{SEE}, is defined as

$$\kappa_{SEE} = \frac{1}{1 + \sum_i \frac{\Omega_i \gamma_i}{Z_i}}. \tag{23}$$

Acknowledgments

This work was supported by a Nasa Space Technology Graduate Research Opportunity (80NSSC23K1187).

References

[1] Goebel, D., and Katz, I., *Fundamentals of Electric Propulsion: Ion and Hall Thrusters*, John Wiley and Sons, 2008.

[2] NASA, "Nasa Space Science Data Coordinate Archive," , 2023. `https://nssdc.gsfc.nasa.gov/nmc/spacecraft/display.action?id=2023-026N` [Accessed: 6/14/24].

[3] Andreussi, T., Ferrato, E., and Giannetti, V., "A review of air-breathing electric propulsion: from mission studies to technology verification," *Journal of Electric Propulsion*, Vol. 1, No. 1, 2022, p. 31.

[4] Su, L., and Jorns, B., "Performance comparison of a 9-kW magnetically shielded Hall thruster operating on xenon and krypton," *Journal of Applied Physics*, Vol. 130, No. 16, 2021.

[5] Marchioni, F., and Capelli, M. A., "Extended Channel Hall Thruster For Airbreathing Propulsion," *Journal of Applied Physics*, 2021.

[6] Su, L. L., Roberts, P. J., Gill, T. M., Hurley, W. J., Marks, T., Sercel, C., Allen, M. G., Whittacker, C. B., Viges, E., and Jorns, B., "High Current Density Operation and Performance of a Magnetically Sheilded Hall Thruster," *Journal of Propulsion and Power*, 2024.

[7] Marks, T. A., and Jorns, B. A., "Challenges with the self-consistent implementation of closure models for anomalous electron transport in fluid simulations of Hall thrusters," *Plasma Sources Science and Technology*, Vol. 32, No. 4, 2023, p. 045016.

[8] Roberts, P. J., and Jorns, B. A., "Laser Measurement of Anomalous Electron Diffusion in a Crossed-Field Plasma," *Physical Review Letters*, Vol. 132, No. 13, 2024, p. 135301.

[9] Cusson, S., Hofer, R., and Lobbia, R., "Performance of the H9 Magnetically Sheilded Hall Thrusters," International Electric Propulsion Conference, Atlanta, Georgia, 2017.

[10] Hofer, R. R., Cusson, S. E., Lobbia, R. B., and Gallimore, A. D., "The H9 Magnetically Shielded Hall Thruster," *35th International Electric Propulsion Conference*, Atlanta, GA, 2017.

[11] Mikellides, I. G., Katz, I., Hofer, R. R., Goebel, D. M., de Grys, K., and Mathers, A., "Magnetic Sheilding of the channel walls in a Hall plasma accelerator," *Physics of Plasmas*, Vol. 18, No. 033501, 2011. https://doi.org/10.1063/1.3551583.

[12] Mikellides, I., Katz, I., Hofer, R., and Goebel, D., "Magnetic Shielding of a Laboratory Hall thruster," *Journal of Applied Physics*, Vol. 115, No. 043303, 2014. https://doi.org/10.1063/1.4862313.

[13] Su, L. L., Gill, T. M., Roberts, P. J., Hurley, W. J., Marks, T., Sercel, C., Allen, M. G., Whittacker, C. B., Byrne, M., Brown, Z., Viges, E., and Jorns, B., "Operation and Performance of a Magnetically Sheilded Hall Thruster at UltraHigh Current Densities Operation on Xenon and Krytpon," *SciTech Forum and Exposition*, 2023.

[14] Peterson, P. Y., Kamhawi, H., Huang, W., Williams, G., Gilland, J. H., Yim, J., Hofer, R. R., and Herman, D. A., "Nasa's Hermes hall thruster electrical configuration characterization," *52nd AIAA/SAE/ASEE Joint Propulsion Conference*, 2016, p. 5027.

[15] Hruby, V., Hohman, K., and Szabo, J., "Air breathing Hall effect thruster design studies and experiments," *37th International Electric Propulsion Conference, Boston, Massachusetts, IEPC-2022-446.*, 2022.

[16] Neumann, A., Hannemann, K., and Brchnelova, M., "Challenges of Cryopumping EP-Propellants in DLR's Electric Propulsion Test Facility," *36th Int. Electric Propulsion Conf*, 2019.

[17] Lobbia, R. B., and Beal, B. E., "Recommended Practice for Use of Langmuir Probes in Electric Propulsion Testing," *Journal of Propulsion and Power*, Vol. 33, No. 3, 2017, pp. 566–581. https://doi.org/10.2514/1.B35531.

[18] Brown, D. L., Walker, M. L., Szabo, J., Huang, W., and Foster, J. E., "Recommended Practice for Use of Faraday Probes in Electric Propulsion Testing," *Journal of Propulsion and Power*, Vol. 33, No. 3, 2017, pp. 582–613. https://doi.org/10.2514/1.B35696.

[19] Hagstrum, H. D., "Auger ejection of electrons from tungsten by noble gas ions," *Physical Review*, Vol. 96, No. 2, 1954, p. 325.

[20] Hagstrum, H. D., "Auger ejection of electrons from molybdenum by noble gas ions," *Physical Review*, Vol. 104, No. 3, 1956, p. 672.

[21] Mahadevan, P., Magnuson, G., Layton, J., and Carlston, C., "Secondary-electron emission from molybdenum due to positive and negative ions of atmospheric gases," *Physical Review*, Vol. 140, No. 4A, 1965, p. A1407.

[22] Huang, W., Shastry, R., Soulas, G. C., and Kamhawi, H., "Fairfield Plume Measurement and Analysis on the NASA-300M and NASA-300MS," *International Electric Propulsion Conference (IEPC)*, 2013.

[23] Hofer, R. R., and Gallimore, A. D., "High-specific impulse Hall thrusters, part 2: efficiency analysis," *Journal of Propulsion and Power*, Vol. 22, No. 4, 2006, pp. 732–740.

[24] Huang, W., and Shastry, R., "Analysis of Wien filter spectra from Hall thruster plumes," *Review of Scientific Instruments*, Vol. 86, No. 7, 2015.

[25] Stebbings, R., Turner, B. R., and Smith, A., "Charge transfer in oxygen, nitrogen, and nitric oxide," *The Journal of Chemical Physics*, Vol. 38, No. 9, 1963, pp. 2277–2279.

[26] Cusson, S. E., Dale, E. T., Jorns, B. A., and Gallimore, A. D., "Acceleration region dynamics in a magnetically shielded Hall thruster," *Physics of Plasmas*, Vol. 26, No. 2, 2019.

[27] Chaplin, V. H., Jorns, B. A., Lopez Ortega, A., Mikellides, I. G., Conversano, R. W., Lobbia, R. B., and Hofer, R. R., "Laser-induced fluorescence measurements of acceleration zone scaling in the 12.5 kW HERMeS Hall thruster," *Journal of Applied Physics*, Vol. 124, No. 18, 2018.

[28] Su, L. L., Marks, T., and Jorns, B. A., "Trends in mass utilization of a magnetically shielded Hall thruster operating on Xenon and Krypton," *Plasma Sources Science and Technology*, 2024.

[29] Dannenmayer, K., and Mazouffre, S., "Elementary scaling laws for sizing up and down Hall effect thrusters: Impact of simplifying assumptions," *Proceedings of the 31st International Electric Propulsion Conference (Ann Arbor), IEPC*, 2009, pp. 09–077.

[30] Mikellides, I. G., Katz, I., Hofer, R. R., and Goebel, D. M., "Magnetic shielding of a laboratory Hall thruster. I. Theory and validation," *Journal of Applied Physics*, Vol. 115, No. 4, 2014.

[31] Hall, S. J., Jorns, B. A., Gallimore, A. D., Kamhawi, H., and Huang, W., "Plasma Plume Characterization of a 100 kW Nested Hall Thruster," *Journal of Propulsion and Power*, Vol. 38, No. 1, 2022, pp. 97–110.

[32] Hofer, R., "Development and Charachterization of High-Efficiency, High-Specific Impulse Xenon Hall Thrusters," Ph.D. thesis, University of Michigan, Ann Arbor, MI, 2004.

[33] Kim, V., "Main physical features and processes determining the performance of stationary plasma thrusters," *Journal of propulsion and power*, Vol. 14, No. 5, 1998, pp. 736–743.